Green synthesis and DFT insight into carbon-doped ZnO nanoparticles derived from rambutan peel for enhanced photocatalytic performance

Tran Do Dat

dodattran09@gmail.com

University of Agriculture and Forestry: Nong Lam University https://orcid.org/0000-0002-2761-5860

Phan Van Qui

University of Agriculture and Forestry: Nong Lam University

Pham Thanh Cong

University of Agriculture and Forestry: Nong Lam University

Nguyen Thi Ngoc Huyen

University of Agriculture and Forestry: Nong Lam University

Dang The Hien

University of Agriculture and Forestry: Nong Lam University

Nguyen Thi Van Anh

University of Agriculture and Forestry: Nong Lam University

Research Article

Keywords: Carbon-doped ZnO, Green synthesis, Rambutan peel extract, Photocatalytic degradation, Density functional theory (DFT)

Posted Date: January 13th, 2026

DOI: https://doi.org/10.21203/rs.3.rs-8091837/v1

Version of Record: A version of this preprint was published at Waste and Biomass Valorization on June 2nd, 2026. See the published version at https://doi.org/10.1007/s12649-026-03684-y.

Green synthesis and DFT insight into carbon-doped ZnO nanoparticles derived from rambutan peel for enhanced photocatalytic performance

Tran Do Dat[1,*], Phan Van Qui[1], Pham Thanh Cong[2], Nguyen Thi Ngoc Huyen[2], Dang The Hien[3]

[1]*Department of Natural Products, Faculty of Chemical Engineering and Food Technology, Nong Lam University, Ho Chi Minh City, Vietnam*

[2]*Faculty of Biological Sciences, Nong Lam University, Ho Chi Minh City, Vietnam*

[3]*Research Institute for Biotechnology and Environment, Nong Lam University, Ho Chi Minh City, Vietnam*

*Corresponding author, e-mail: dat.trando@hcmuaf.edu.vn

Abstract

In this study, carbon-doped ZnO nanoparticles (C–ZnO) were successfully synthesized through a green route using rambutan (*Nephelium lappaceum* L.) peel extract as a natural reducing, stabilizing, and carbon source. The effects of calcination temperature on the structural, morphological, and optical properties of the as-prepared samples were systematically investigated. XRD and Raman analyses confirmed the formation of wurtzite ZnO with embedded graphitic carbon, while FTIR spectra indicated the coexistence of Zn–O and carbon-related functional groups. The optimal sample calcined at 600 °C exhibited a balanced crystallinity, uniform morphology, and moderate carbon incorporation, leading to an optimal band gap of 3.08 eV and superior photocatalytic activity toward methylene blue (MB) degradation under UV irradiation. The photocatalytic efficiency was strongly influenced by operational factors such as pH, dye concentration, and catalyst dosage, with the best performance obtained at pH 11, 10 mg L^{-1} MB, and 50 mg catalyst dosage. Radical scavenging experiments confirmed that both •OH and h^+ radicals were the dominant reactive species. DFT calculations revealed that carbon doping narrowed the band gap by introducing C 2p–O 2p hybridized states and promoted charge redistribution within the ZnO lattice, which enhanced visible-light absorption and charge separation. The combined experimental and theoretical findings demonstrate that biomass-derived carbon doping is an effective strategy to tune the electronic structure of ZnO, leading to high photocatalytic efficiency and excellent reusability, offering a sustainable pathway for environmental remediation.

Keyword: Carbon-doped ZnO; Green synthesis; Rambutan peel extract; Photocatalytic degradation; Density functional theory (DFT)

1. Introduction

The discharge of dye-containing wastewater from textile, leather, and printing industries has become a serious environmental issue worldwide [1]. Synthetic dyes such as methylene blue (MB) are

widely applied due to their low cost, stability, and strong coloration, but they are poorly biodegradable and toxic to aquatic organisms [2]. The persistence of MB in natural waters blocks sunlight penetration, inhibits photosynthesis, lowers oxygen levels, and poses risks to human health and aquatic ecosystems [3]. As a result, developing effective and sustainable technologies for the removal of MB from wastewater remains an urgent challenge.

Heterogeneous photocatalysis is considered a promising technology because it can mineralize organic contaminants into harmless products such as carbon dioxide and water under light irradiation [4,5]. Semiconductor photocatalysts generate electron–hole pairs when excited by light, which participate in redox reactions to produce reactive oxygen species capable of degrading pollutants [6]. Zinc oxide (ZnO) is one of the most attractive photocatalysts owing to its wide band gap of about 3.3 eV, strong ultraviolet absorption, high chemical stability, low toxicity, and low cost [7,8]. However, pristine ZnO suffers from limited photocatalytic efficiency due to fast electron–hole recombination and poor utilization of visible light [9]. These shortcomings restrict its practical application in environmental remediation.

Several modification strategies have been developed to improve the photocatalytic efficiency of ZnO, including heterojunction formation, surface functionalization, and element doping. Among them, carbon doping is especially effective [10]. The introduction of carbon atoms into the ZnO lattice can generate intermediate energy states, reduce the band gap, extend light absorption into the visible region, and improve charge carrier separation [11]. These effects significantly enhance photocatalytic efficiency by facilitating the generation of reactive oxygen species. Consequently, carbon-doped ZnO has been widely studied as a multifunctional material with potential applications in both environmental treatment and antibacterial protection.

The synthesis route plays a critical role in determining the structural, optical, and surface properties of ZnO as well as the environmental safety of the process. Conventional chemical synthesis often requires hazardous reducing or stabilizing agents and may generate toxic by-products, which raise concerns about cost, safety, and scalability [12]. In contrast, green synthesis using plant extracts has emerged as a sustainable and eco-friendly approach [13,14]. Plant-derived biomolecules such as polyphenols, flavonoids, and tannins can serve simultaneously as reducing and capping agents, allowing nanoparticles to form under mild and environmentally benign conditions [15].

Rambutan (*Nephelium lappaceum* L.) peel is an abundant agricultural by-product in tropical regions that is typically discarded as waste despite being rich in valuable phytochemicals [16]. Utilizing rambutan peel extract for ZnO synthesis provides a renewable and low-cost alternative to conventional reagents. More importantly, the organic components of rambutan peel can also act as an intrinsic carbon source during calcination, enabling in situ carbon doping of ZnO. This dual role, in which the extract

functions both as a green reducing agent and as a natural dopant precursor, creates an innovative pathway that combines waste valorization with the development of advanced photocatalysts. Such a strategy supports sustainable development and circular economy principles while simultaneously enhancing the performance of ZnO-based materials [11].

In addition to photocatalytic dye degradation, ZnO nanoparticles are well known for their antibacterial properties against Gram-positive and Gram-negative bacteria. The antibacterial mechanism involves the production of reactive oxygen species, membrane disruption, and interference with cellular processes. Carbon incorporation further promotes these effects by enhancing electron transfer and increasing reactive oxygen species generation [17]. As a result, rambutan peel mediated carbon doped ZnO nanoparticles are expected to provide dual functionality for both wastewater purification and antibacterial applications.

Despite these promising aspects, systematic studies that integrate green synthesis, biomass-derived carbon doping, photocatalytic activity, antibacterial evaluation, recyclability, and theoretical modeling remain limited. Operational factors such as calcination temperature, solution pH, dye concentration, and catalyst dosage also exert strong influence on photocatalytic performance, yet their combined effects on green synthesized carbon doped ZnO have not been thoroughly examined. Moreover, a deeper understanding of the photocatalytic mechanism requires correlation between experimental results and electronic structure analyses.

Density functional theory (DFT) provides a powerful tool to achieve this correlation. By analyzing the effect of carbon incorporation on band structure, band gap narrowing, and electron density distribution, DFT offers insights into charge transfer pathways and explains the origin of enhanced photocatalytic activity [18]. Combining theoretical simulations with experimental investigations enables a comprehensive understanding of material behavior and supports the rational design of efficient photocatalysts.

In this study, carbon doped ZnO nanoparticles were synthesized using rambutan peel extract as both a natural reducing and stabilizing agent and as a source of carbon for doping. The prepared materials were characterized by X-ray diffraction, Fourier transform infrared spectroscopy, scanning electron microscopy with energy dispersive X-ray analysis, ultraviolet–visible diffuse reflectance spectroscopy, photoluminescence, and Raman spectroscopy to evaluate their structural, morphological, and optical properties. Photocatalytic degradation of methylene blue under ultraviolet irradiation was systematically investigated by varying calcination temperature, pH, dye concentration, and catalyst dosage. The recyclability and long-term stability of the catalysts were assessed through repeated cycles. Furthermore, DFT simulations were performed to provide theoretical insight into the electronic structure of carbon doped ZnO and to validate experimental findings.

2. Materials and Methods

2.1. Materials

Fresh rambutan (*Nephelium lappaceum* L.) peels were collected from a local source, washed thoroughly, and used to prepare aqueous extract. Zinc acetate dihydrate ($Zn(CH_3COO)_2 \cdot 2H_2O$, silver nitrate ($AgNO_3$), analytical grade), sodium hydroxide (NaOH), and methylene blue (MB) were purchased from Merck. All chemicals were of analytical grade and used without further purification. Deionized (DI) water was used throughout.

2.2 Preparation of rambutan peel extract

Approximately 20 g of dried rambutan peel was boiled in 200 mL DI water at 80 °C for 30 min. The solution was filtered through Whatman No. 1 filter paper, cooled, and stored at 4 °C for further use. The extract contains polyphenols and tannins which act as reducing and stabilizing agents, and also serve as a natural carbon source during calcination.

2.3 Synthesis of carbon doped ZnO nanoparticles

The synthesis of carbon doped ZnO was carried out with slight modifications based on a previously reported method [19]. Zinc acetate solution (0.1 M) was prepared and mixed with rambutan peel extract under stirring. Aqueous NaOH solution (1 M) was then added dropwise until pH reached approximately 10, leading to the formation of a white precipitate. The precipitate was collected by centrifugation, washed repeatedly with DI water and ethanol to remove residual ions, and dried at 80 °C overnight. The dried powders were calcined at 400, 600, and 800 °C for 2 h to obtain ZnO nanoparticles with varying carbon incorporation levels.

2.4 Characterization

The phase structure was determined by X-ray diffraction (XRD, Cu Kα radiation). Functional groups were identified using Fourier transform infrared spectroscopy (FT-IR, 400–4000 cm^{-1}). The morphology and composition were analyzed by scanning electron microscopy with energy dispersive X-ray analysis (SEM-EDX). Optical properties were examined by ultraviolet–visible diffuse reflectance spectroscopy (UV–Vis DRS, 200–800 nm), photoluminescence (PL, excitation 325 nm), and Raman spectroscopy. The band gap energy was estimated from Tauc plots derived from UV–Vis spectra.

2.5 Photocatalytic activity and kinetics

Photocatalytic degradation of MB was conducted under UV irradiation (365 nm). In a typical experiment, 50 mL of MB solution (10 mg/L) was mixed with 50 mg of catalyst in a quartz reactor. Prior to irradiation, the suspension was magnetically stirred in the dark for 30 min to reach adsorption–desorption

equilibrium. At fixed time intervals, aliquots of 3 mL were withdrawn, centrifuged, and analyzed using UV–Vis spectrophotometry at 664 nm. The degradation efficiency (H) was calculated as Equation (1):

$$H\ (\%) = \left(1 - \frac{C_t}{C_o}\right) \times 100\ \% \quad (1)$$

where C_0 and C_t are the initial and time-dependent MB concentrations, respectively.

To investigate the kinetics, the experimental data were fitted to both pseudo-first-order kinetic models. The rate constants (k) were obtained from linear fitting of $\ln(C_0/C_t)$ versus t (pseudo-first-order).

2.6 Radical trapping experiments and mechanism study

To identify the main reactive species involved in photocatalysis, radical trapping experiments were performed by adding specific scavengers: isopropanol (•OH scavenger), p-benzoquinone ($\bullet O_2^-$ scavenger), $AgNO_3$ (e^- scavenger), and EDTA (h^+ scavenger) into the MB solution under identical conditions. The change in photocatalytic activity with each scavenger was used to clarify the dominant degradation pathway.

2.7 Recyclability and stability

To evaluate catalyst reusability, the photocatalytic degradation of MB was repeated for four consecutive cycles. After each cycle, the catalyst was recovered by centrifugation, washed thoroughly with DI water, dried at 80 °C, and reused without further modification. The retention of photocatalytic efficiency was used to assess stability.

2.9 Density functional theory calculations

Density functional theory (DFT) calculations were conducted using the CASTEP module implemented in Materials Studio to investigate the electronic properties of pristine and carbon-doped ZnO. The generalized gradient approximation (GGA) with the Perdew–Burke–Ernzerhof (PBE) exchange–correlation functional was employed. Geometry optimization was performed under the Fine convergence tolerance, with thresholds of 1.0×10^{-5} eV/atom for total energy, 0.03 eV/Å for maximum force, 0.05 GPa for maximum stress, and 0.001 Å for maximum displacement. The energy cutoff for plane-wave expansion was set to 400 eV, and the Monkhorst–Pack k-point grid was defined as 4 × 4 × 3. Koelling–Harmon relativistic treatment and ultrasoft pseudopotentials (OTFG type) were adopted. The spin polarization was set to non-polarized, and van der Waals interactions were corrected using the TS dispersion scheme.

Supercells of pure ZnO and carbon-substituted ZnO were constructed to evaluate the influence of carbon incorporation on the crystal and electronic structures. After full geometry optimization, the band structure, density of states (DOS), and electron density difference (EDD) were computed to analyze the

effect of carbon doping on band gap narrowing, charge redistribution, and electronic transition behavior. These theoretical results were correlated with experimental UV–Vis DRS and PL data to elucidate the mechanism of enhanced photocatalytic activity.

3. Results and discussion

3.1. Characterization of C-ZnO

The XRD patterns of the C–ZnO samples calcined at different temperatures (400, 600, and 800 °C) confirm the formation of hexagonal wurtzite ZnO (JCPDS No. 46-1451) without any detectable impurity phases (Figure 1) [20]. The diffraction peaks at $2\theta = 31.7°$, 34.4°, and 36.2° correspond to the (100), (002), and (101) planes, respectively. As the calcination temperature increased, the peaks became sharper and more intense, indicating an improvement in crystallinity and an increase in crystallite size.

At 400 °C, the broad diffraction peaks and weak intensity suggest the presence of poorly crystallized ZnO mixed with amorphous carbonaceous residues derived from rambutan-peel extract. The partial carbon coating at this stage inhibits full crystallization, which can limit charge transport. When the calcination temperature reached 600 °C, the peaks became well-defined, implying optimal crystal growth and partial removal of excess carbon. Such a balance between crystallinity and surface carbon content is beneficial for photocatalysis: the carbon species enhance visible-light absorption and promote charge separation, while the well-crystallized ZnO lattice facilitates efficient electron transfer. Consequently, the C–ZnO–600 sample exhibited the highest photocatalytic activity toward methylene blue degradation.

In contrast, the sample calcined at 800 °C displayed the sharpest peaks, corresponding to highly crystalline ZnO with minimal carbon residues. However, excessive grain growth at this temperature reduces the surface area and the number of surface defects, leading to decreased adsorption and fewer active sites for photocatalytic reactions. Therefore, the superior performance of C–ZnO–600 can be attributed to its synergistic structure combining sufficient crystallinity, moderate carbon content, and a high density of surface-active sites.

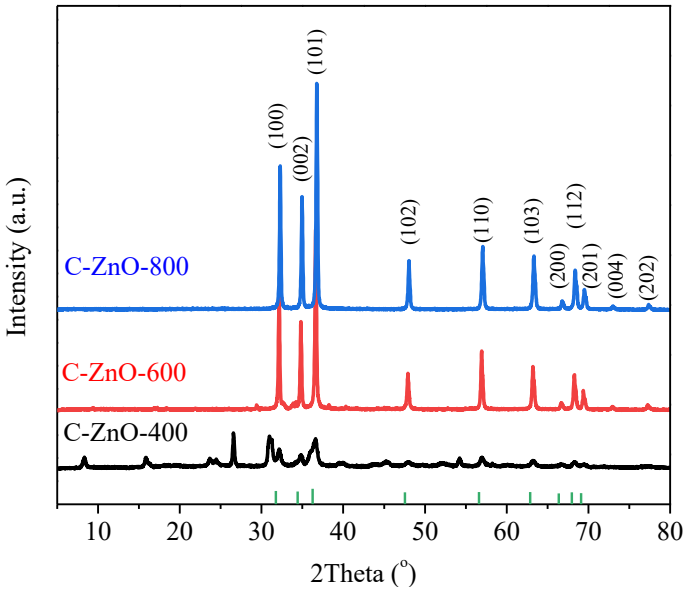

Figure 1: XRD patterns of the C-ZnO at various temperatures

The FTIR spectra of the C–ZnO materials (Figure 2) exhibit characteristic vibrational modes confirming the coexistence of ZnO and carbonaceous species derived from the rambutan-peel extract. The broad absorption band at around 3400 cm^{-1} corresponds to O–H stretching vibrations of adsorbed water and surface hydroxyl groups [21]. The peaks near 1400 cm^{-1} are assigned to C–O–H bending vibration [20], respectively, indicating the presence of residual carbon and nitrogen functionalities originating from biomolecules in the extract. The weak band at 1090 cm^{-1} is associated with C–H stretching, indicating the presence of residual carbon and nitrogen functionalities originating from biomolecules in the extract [22], while the strong absorption below 600 cm^{-1} corresponds to the Zn–O stretching vibration, confirming the formation of ZnO [20].

As the calcination temperature increased, the intensity of organic-related bands decreased, demonstrating progressive removal of carbonaceous residues. For C–ZnO–600, the balanced intensity of Zn–O and C–N/C=O bands suggests a moderate carbon incorporation that can facilitate charge transfer and improve photocatalytic efficiency.

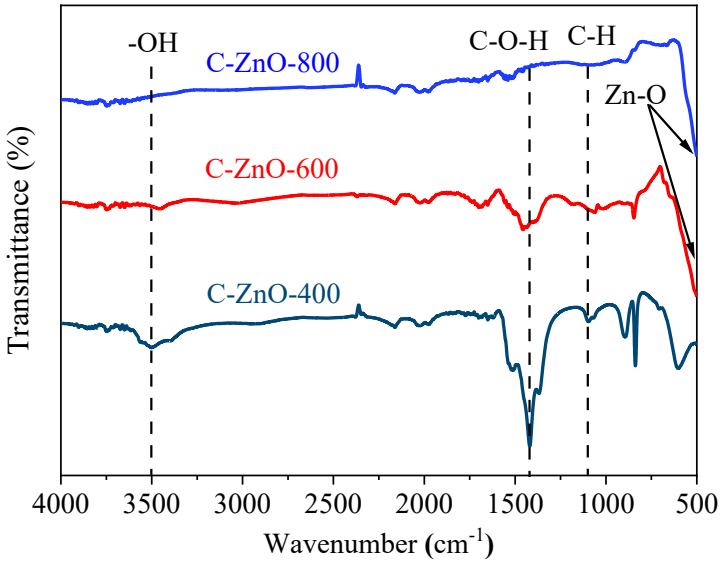

Figure 2: FTIR spectra of materials

Figure 3 presents the Raman spectra of the carbon-doped ZnO photocatalyst synthesized using rambutan peel extract. Several characteristic modes of wurtzite ZnO are observed, including E_2(low) (101 cm^{-1}), A_1(TO) (384.8 cm^{-1}), E_2(high) (435.6 cm^{-1}), and E_1(LO) (583.1 cm^{-1}) [23]. The clear presence of the E_2(low) and E_2(high) modes, often referred to as the E_2(high)–E_2(low) pair, confirms the retention of the hexagonal wurtzite structure with high crystallinity after carbon incorporation. The A_1(TO) mode exhibits very weak intensity, while the E_1(LO) mode is slightly more intense but still moderate, indicating that carbon doping introduces only mild lattice strain without significant distortion of the ZnO crystal framework [24].

In addition to ZnO-related peaks, two distinct carbon-related bands appear at approximately 1340 cm^{-1} (D band) and 1585 cm^{-1} (G band). The D band corresponds to disordered or defect-induced vibrations of sp^3 carbon, whereas the G band represents the stretching vibrations of sp^2-bonded carbon atoms in graphitic domains [25]. The higher intensity of the G band ($(I_D/I_G) < 1$) suggests that the incorporated carbon exhibits a relatively ordered graphitic structure with few structural defects. Such a configuration is advantageous for photocatalytic processes, as graphitic carbon can enhance charge transport, facilitate electron–hole separation, and expand light absorption through π–π conjugation [26]. The Raman analysis demonstrates that carbon atoms are successfully incorporated into ZnO without disrupting the wurtzite phase. The coexistence of crystalline ZnO modes and graphitic carbon features indicates the formation of a C–ZnO composite with synergistic structural and electronic properties, which is expected to significantly enhance photocatalytic activity.

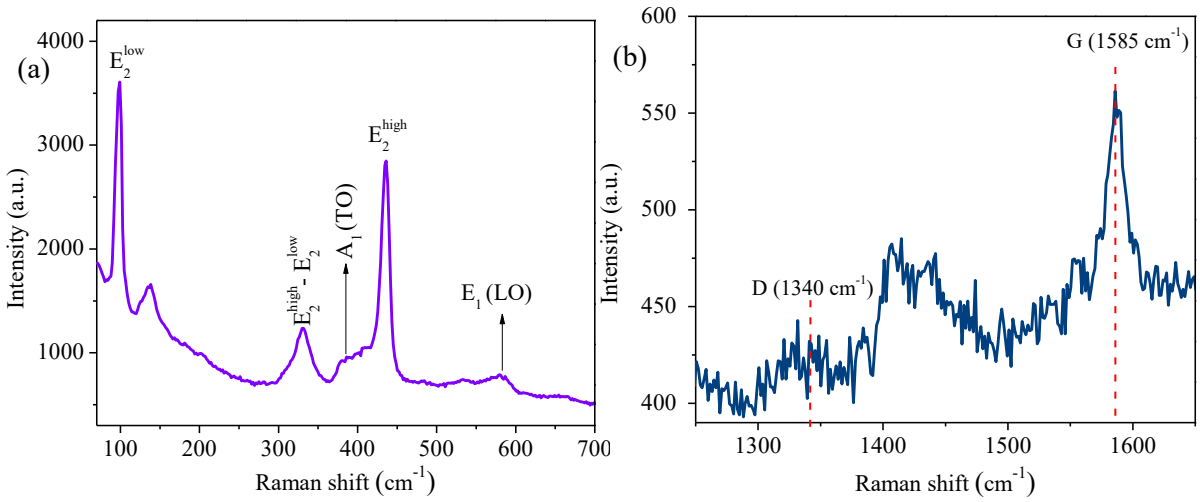

Figure 3: Raman spectrum of C-ZnO-600

The EDS elemental mapping images of the C–ZnO samples calcined at different temperatures (400, 600, and 800 °C) are presented in Fig. 4(a–c). The mappings clearly show the homogeneous distribution of Zn (red), O (cyan), and C (yellow) elements throughout the composite, indicating the successful incorporation of carbon species within the ZnO matrix. At 400 °C, the carbon signal is relatively strong and uniformly dispersed on the surface, suggesting the presence of abundant carbonaceous residues from the precursor. As the calcination temperature increases to 600 °C and 800 °C, the intensity of the carbon signal gradually decreases, implying partial oxidation or removal of surface carbon species during thermal treatment, while Zn and O signals become more dominant and well-defined.

The corresponding EDS spectra (Fig. 4d) confirm the presence of Zn, O, and C in all samples, with quantitative results summarized in the inset table. The Zn content increases with temperature, from 54.3 wt% at 400 °C to 75.6 wt% at 800 °C, whereas the carbon proportion decreases from 13.8 wt% to 7.4 wt%. This trend suggests that higher calcination temperature promotes crystallization and densification of ZnO while reducing the amount of surface carbon. Overall, the EDS mapping and compositional data verify that carbon is successfully doped into ZnO, and its distribution and concentration are strongly affected by the calcination temperature.

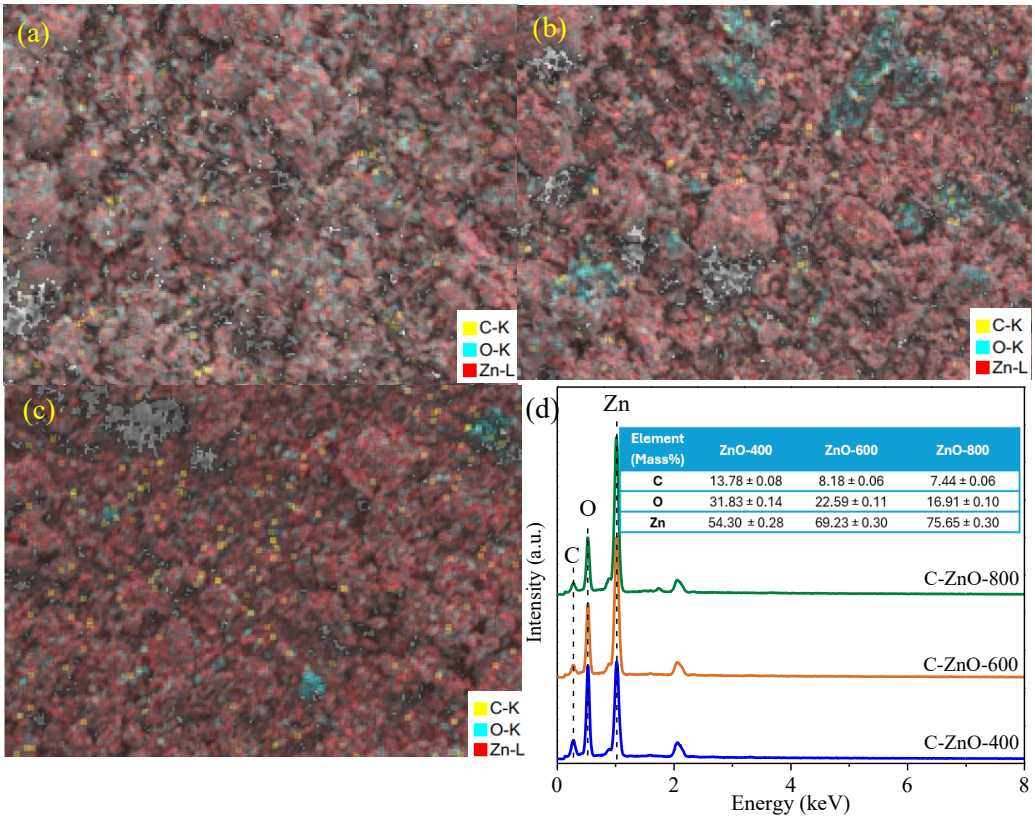

Element (Mass%)	ZnO-400	ZnO-600	ZnO-800
C	13.78 ± 0.08	8.18 ± 0.06	7.44 ± 0.06
O	31.83 ± 0.14	22.59 ± 0.11	16.91 ± 0.10
Zn	54.30 ± 0.28	69.23 ± 0.30	75.65 ± 0.30

Figure 4: Elemental mapping and EDS analysis of C–ZnO samples calcined at 400, 600, and 800 °C

The surface morphologies of the C–ZnO composites calcined at different temperatures are illustrated in Fig. 5(a–c). At 400 °C, the sample exhibits a plate-like and rod-like structure with sharp edges, indicating incomplete crystallization of ZnO. When the temperature increases to 600 °C, the particles become more compact and uniform, forming spherical-like agglomerates with an average size of approximately 247.94 ± 14.25 nm, as shown in Fig. 5(d). This morphology suggests enhanced crystallinity and particle fusion due to the sintering effect. However, further calcination at 800 °C leads to the formation of larger, densely packed aggregates, which can be attributed to excessive grain growth and coalescence [27,28].

The evolution of morphology with increasing temperature clearly demonstrates the strong influence of thermal treatment on the nucleation and growth behavior of C–ZnO particles. The reduction in surface area at higher temperatures may hinder photocatalytic efficiency, despite improved crystallinity. Therefore, the sample calcined at 600 °C was selected for subsequent optical and photocatalytic analyses, as it exhibits an optimal balance between particle uniformity and surface activity.

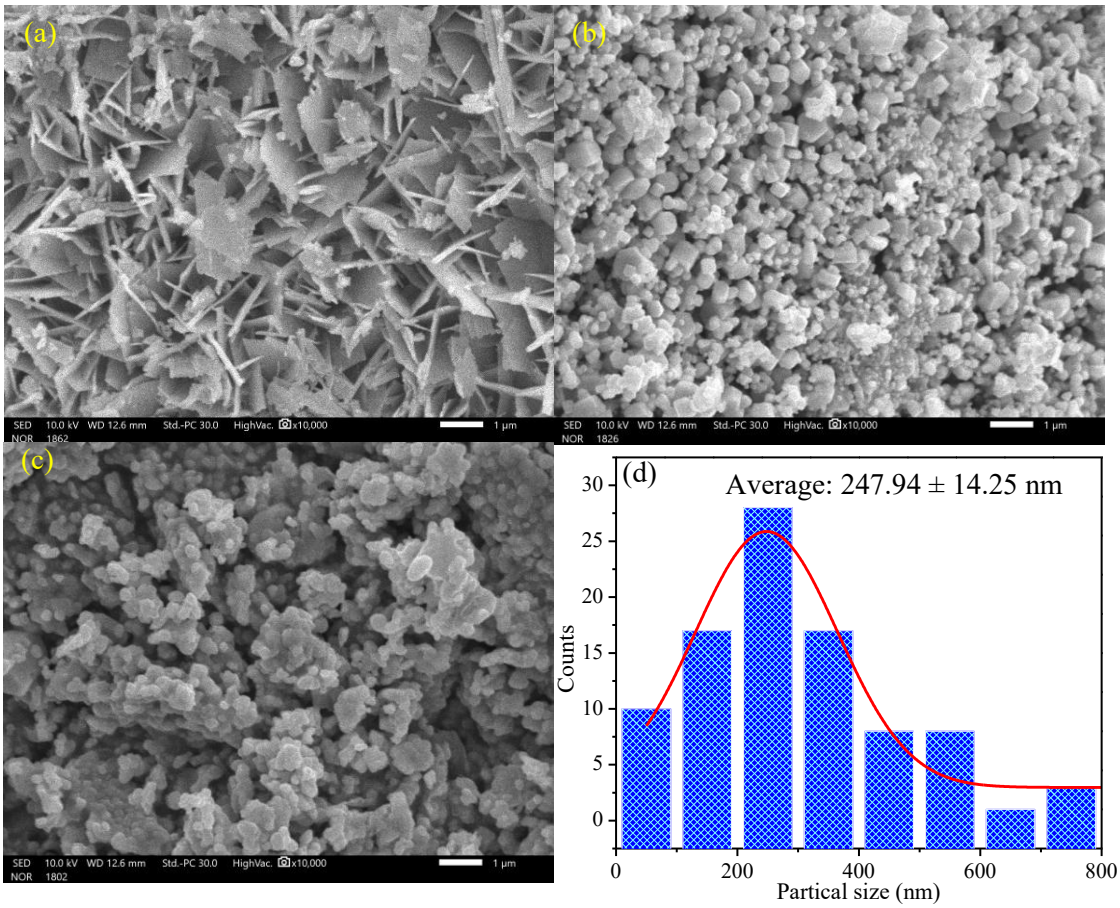

Figure 5: SEM images of C–ZnO samples calcined at different temperatures: (a) C–ZnO–400, (b) C–ZnO–600, (c) C–ZnO–800, and (d) particle size distribution of C–ZnO–600

Figure 6(a) presents the photoluminescence (PL) spectra of carbon-doped ZnO (C–ZnO) samples calcined at different temperatures (400, 600, and 800 °C). All samples exhibit a strong near-band-edge (NBE) UV emission centered around 395 nm, which is attributed to the excitonic recombination of electrons and holes in the ZnO lattice [29]. In addition, a broad visible emission band ranging from 450 to 600 nm is observed, arising from deep-level transitions associated with intrinsic (oxygen vacancies, V_O) and extrinsic (zinc interstitials, Z_{ni}) defects [30]. Among the tested samples, C–ZnO–600 displays the most intense and broadened visible emission near 550 nm, indicating a balanced presence of radiative defect centers and optimal crystallinity [31]. This broadening suggests that moderate carbon incorporation introduces multiple defect-related recombination pathways, which extend carrier lifetimes while preserving visible-light responsiveness, consistent with its enhanced photocatalytic performance [32]. In contrast, the weak PL intensity of C–ZnO–400 is ascribed to its poor crystallinity and incomplete defect activation, whereas the quenched emission of C–ZnO–800 results from defect annihilation and grain coarsening at high temperature. Therefore, the intermediate PL intensity of C–ZnO–600 implies an optimal defect density that effectively suppresses electron–hole recombination without compromising radiative transitions.

As shown in Figure 6(b), the CIE 1931 chromaticity coordinates of all samples fall within the blue–green region, consistent with their PL emission colors. A gradual shift of color coordinates from the bluish region (C–ZnO–400) toward green (C–ZnO–800) reflects the evolution of defect-related emission and band-gap modification induced by carbon doping and thermal treatment. This trend corresponds well with the PL broadening around 550 nm, suggesting the formation of carbon-induced mid-gap states that enhance visible-light absorption. The close correlation between the PL spectra and CIE coordinates confirms that a moderate calcination temperature (600 °C) yields an optimal structural–defect balance, favoring efficient charge carrier separation, optical tunability, and superior photocatalytic activity.

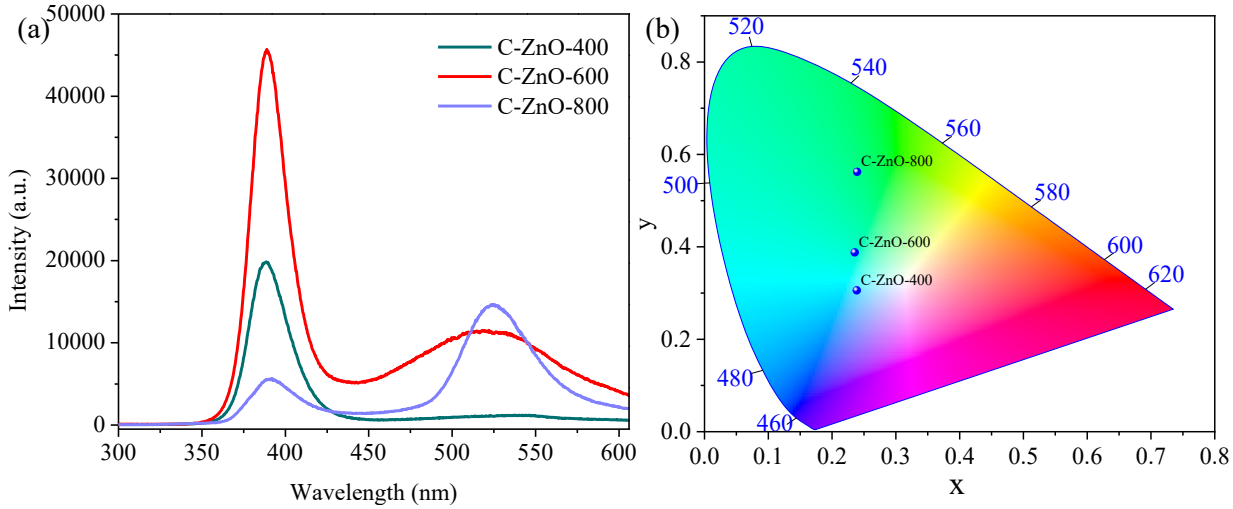

Figure 6: (a) PL spectra and (b) CIE plot of materials

3.2. Photocatalytic degradation and mechanism

3.2.1. Effect of various factors on the degradation efficiency of MB

3.2.1.1. Calcination temperature

The photocatalytic degradation of methylene blue (MB) under UV irradiation was investigated to evaluate the influence of calcination temperature on the activity of the C–ZnO samples (Figure 7a). The degradation efficiency increased with reaction time for all samples, with C–ZnO–600 exhibiting the highest activity, achieving approximately 82% degradation after 180 min. In comparison, the C–ZnO–400 and C–ZnO–800 samples showed lower efficiencies of 68% and 53%, respectively.

This trend reflects the crucial role of calcination temperature in controlling the structural and surface features of the materials. At 400 °C, the ZnO crystals were poorly developed and partially covered by residual carbon, which hindered light absorption and charge transport. At 800 °C, excessive crystal growth caused particle aggregation and reduced surface area, limiting the number of active sites [9]. The sample calcined at 600 °C exhibited an optimal balance between crystallinity, surface area, and moderate

carbon incorporation, enabling more efficient photogenerated charge separation and transfer under UV excitation.

The degradation kinetics followed the pseudo-first-order model based on the Langmuir–Hinshelwood mechanism (Figure 7b). The apparent rate constants (k) were 0.0046, 0.0084, and 0.0041 min^{-1} for C–ZnO–400, C–ZnO–600, and C–ZnO–800, respectively. The rate constant for C–ZnO–600 was nearly double that of the other samples, confirming its superior reaction rate under UV light. This enhancement arises from the synergistic effect of well-crystallized ZnO domains, an appropriate amount of surface carbon, and a moderate density of oxygen vacancies, which collectively facilitate electron–hole generation and suppress recombination. Overall, the results demonstrate that 600 °C is the optimal calcination temperature for achieving a favorable structural–electronic configuration, resulting in the highest photocatalytic efficiency and fastest degradation kinetics under UV irradiation.

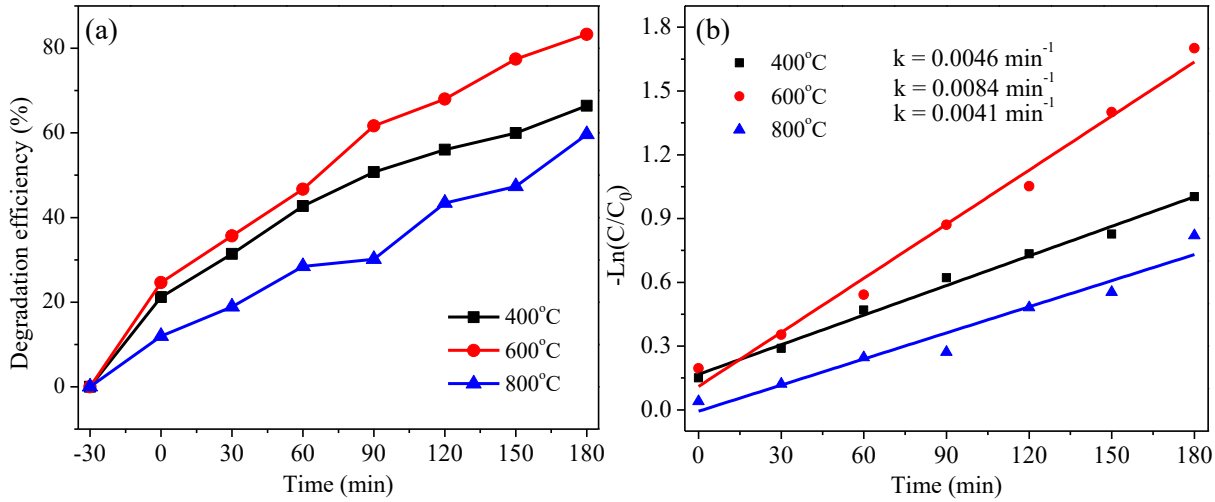

Figure 7: (a) Effect of calcination temperature on the MB photodegradation efficiency and (b) kinetic model of the investigated materials

3.2.1.2. Calcination time

The effect of calcination time on the photocatalytic performance of the C–ZnO samples was investigated through the degradation of methylene blue (MB) under UV irradiation (Figure 8a). The photocatalytic efficiency increased with prolonged calcination up to 6 h and then decreased with further heating. Specifically, the C–ZnO sample calcined for 6 h achieved the highest MB degradation of approximately 82% after 180 min, while samples treated for 4 h and 8 h showed lower efficiencies of 66% and 71%, respectively.

This behavior can be explained by the microstructural evolution during thermal treatment. Insufficient calcination time (4 h) results in incomplete decomposition of organic residues from the rambutan-peel extract and the formation of poorly crystallized ZnO, leading to a high density of surface defects that promote charge recombination. Extending the calcination to 6 h provides adequate energy for

full crystallization and uniform carbon incorporation, forming well-defined nanoparticles with an optimal density of oxygen vacancies and carbon-related surface states that facilitate charge separation and light absorption. However, excessive heating for 8 h induces grain growth and sintering, reducing surface area and active sites available for photocatalytic reactions [33].

The kinetic results (Figure 8b) follow the pseudo-first-order model, consistent with the Langmuir–Hinshelwood mechanism. The apparent rate constants (k) for the samples calcined for 4, 6, and 8 h were 0.0046, 0.0084, and 0.0041 min^{-1}, respectively. The C–ZnO sample calcined for 6 h exhibited a reaction rate nearly twice that of the other two samples, confirming that an intermediate calcination duration yields the most efficient photocatalyst.

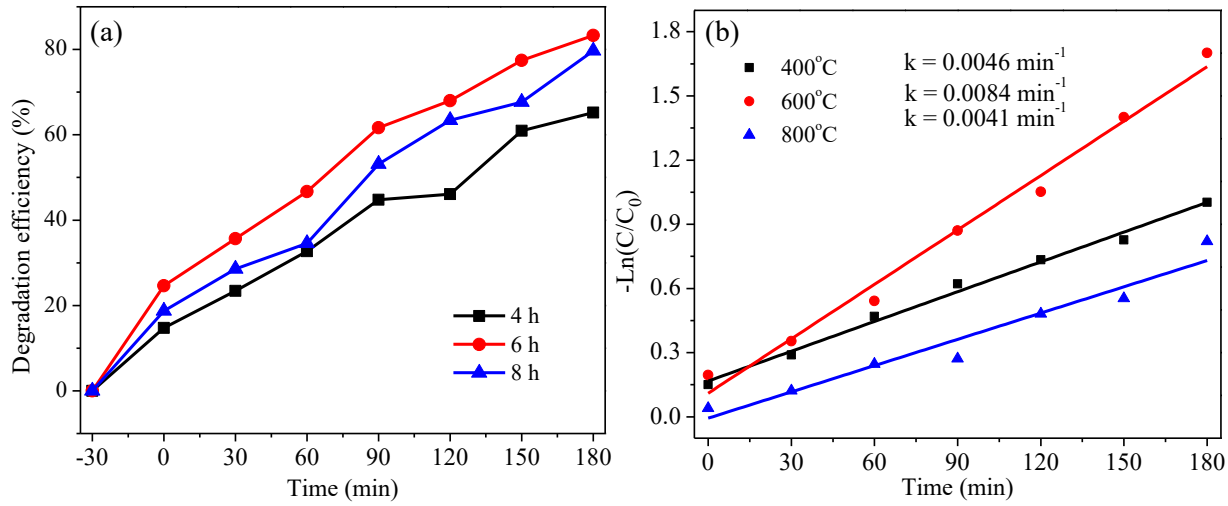

Figure 8: (a) Effect of calcination time on the MB photodegradation efficiency and (b) kinetic model of the investigated materials

3.2.1.3. Catalyst dosage

The influence of catalyst dosage on the UV-induced degradation of methylene blue (MB) was examined using 30, 50, and 70 mg of C–ZnO–600 (Figure 9a). The degradation efficiency increased significantly with catalyst loading up to 50 mg, achieving about 83% removal after 180 min. When the dosage was further raised to 70 mg, only a marginal improvement was observed during the early stage, followed by a slower rate of degradation.

This behavior arises from the interplay between photon absorption and particle dispersion. At low dosage (30 mg), the limited number of active sites restricts the generation of photoinduced charge carriers. Introducing more catalyst (50 mg) ensures adequate photon utilization and efficient contact between MB molecules and reactive sites. However, excessive catalyst (70 mg) causes light scattering and shielding effects, which hinder the penetration of UV light and reduce the effective reaction zone. Therefore, an optimum catalyst concentration is required to maintain a balance between surface accessibility and light harvesting.

The kinetic analysis (Figure 9b) revealed that all reactions followed pseudo-first-order behavior according to the Langmuir–Hinshelwood model. Among the tested samples, the 50 mg dosage exhibited the steepest slope in the kinetic plot, reflecting the most efficient charge utilization during photocatalysis. Both lower and higher dosages resulted in noticeably slower reaction rates due to limited photon absorption or particle agglomeration.

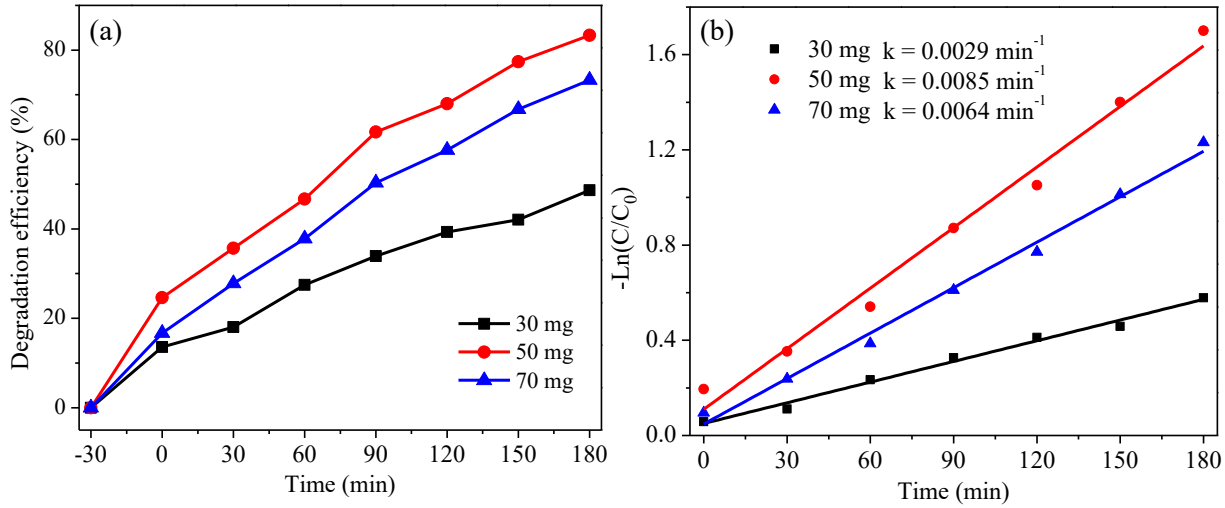

Figure 9: (a) Effect of catalyst dosage on the photodegradation efficiency of methylene blue (MB) and (b) the kinetic model of the investigated materials

3.2.1.4. MB concentration

The influence of initial methylene blue (MB) concentration on the photocatalytic degradation efficiency of the C–ZnO–600 sample under UV light is illustrated in Figure (10a). A clear decline in degradation efficiency was observed as the dye concentration increased from 10 to 20 ppm. After 180 min of irradiation, the removal efficiency decreased from 83% at 10 ppm to 69% at 15 ppm and 52% at 20 ppm.

This inverse relationship can be explained by the competition between photon absorption and dye coverage on the catalyst surface. At lower concentrations, UV light readily reaches the catalyst surface, enabling the generation of abundant electron–hole pairs and the formation of reactive radicals (•OH and $•O_2^-$). As the concentration increases, MB molecules absorb a significant portion of the UV light before it reaches the catalyst surface, while excessive adsorption of dye molecules blocks active sites, thereby suppressing charge transfer and reducing photocatalytic efficiency [34].

The kinetic plots (Figure 10b) confirm pseudo-first-order behavior for all concentrations. The apparent rate constants (k) were 0.0085, 0.0086, and 0.0028 min^{-1} for MB concentrations of 10, 15, and 20 ppm, respectively. Although the 10 and 15 ppm solutions show comparable rate constants, the 20 ppm system exhibits a pronounced kinetic slowdown, indicating mass-transfer limitations and restricted photon penetration at higher dye loadings.

Therefore, maintaining a moderate MB concentration (around 10–15 ppm) ensures an optimal balance between light absorption and reactant availability, allowing efficient utilization of photogenerated charge carriers and achieving the best degradation kinetics under UV irradiation.

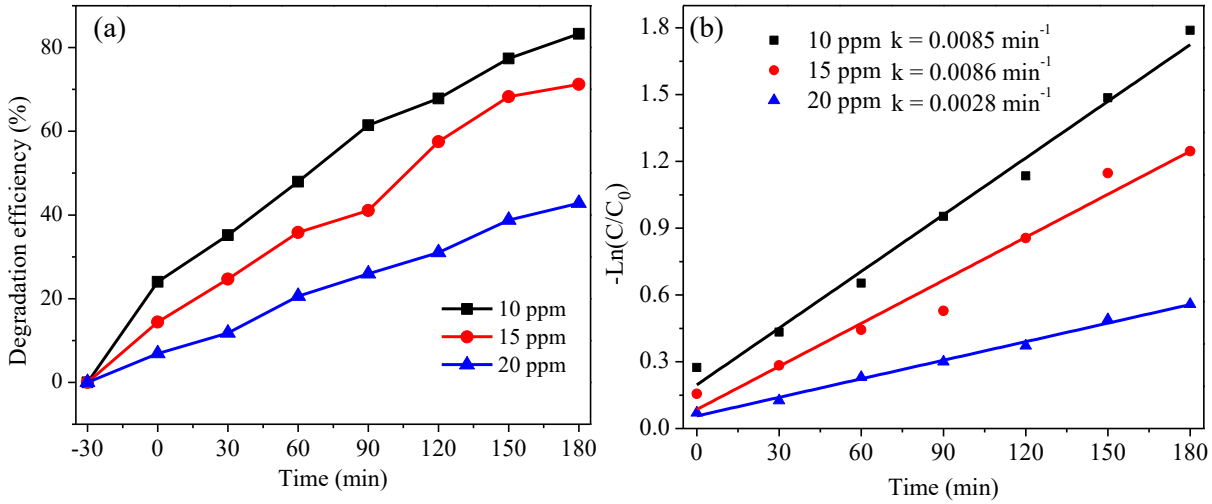

Figure 10: (a) Effect of MB concentration on the photodegradation efficiency of methylene blue (MB) and (b) the kinetic model of the investigated materials

3.2.1.5. pH

The initial pH of the reaction medium plays a decisive role in governing the photocatalytic degradation of methylene blue (MB) by C–ZnO–600, as shown in Figure (11a). A remarkable enhancement in degradation efficiency was observed as the pH increased from 3 to 11. At acidic pH, the degradation was minimal (approximately 30% at pH 3), whereas under alkaline conditions (pH 11) nearly complete removal of MB was achieved within 120 min.

This pronounced pH dependence can be interpreted in terms of surface charge behavior and dye ionization. MB is a cationic dye, and the surface of ZnO becomes positively charged at low pH due to protonation, leading to strong electrostatic repulsion between the dye molecules and the catalyst surface, thus suppressing adsorption and radical generation. As the pH increases, deprotonation of surface hydroxyl groups occurs, rendering the surface negatively charged. This condition enhances the electrostatic attraction toward cationic MB, improving adsorption and facilitating photogenerated charge transfer. Additionally, in alkaline media, a higher concentration of OH^- ions promotes the generation of •OH radicals through oxidation by photogenerated holes, which further accelerates dye degradation [35].

The kinetic data (Figure 11b) followed a pseudo-first-order model with apparent rate constants of 0.0019, 0.0058, 0.0151, 0.0240, and 0.0245 min^{-1} for pH 3, 5, 7, 9, and 11, respectively. The rate constant increased almost exponentially with pH, stabilizing beyond pH 9, suggesting that excessive alkalinity offers no further advantage once the ZnO surface becomes fully deprotonated.

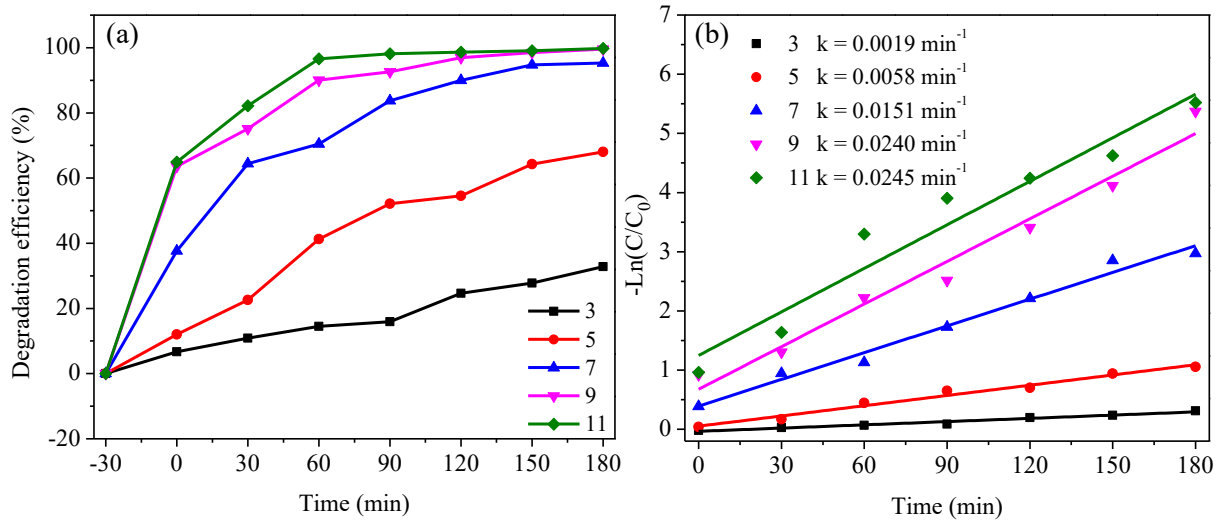

Figure 11: (a) Effect of pH on the photodegradation efficiency of methylene blue (MB) and (b) the kinetic model of the investigated materials

Table 1 summarizes and compares the photocatalytic degradation efficiency of methylene blue (MB) using C–ZnO–600 and other reported ZnO-based catalysts under various operating conditions. As presented, the C–ZnO–600 sample exhibited a remarkably high degradation efficiency of 99.75% under UV illumination at pH 11, which is comparable to or even slightly higher than most previously reported ZnO-based photocatalysts. In contrast, the pure ZnO and metal-doped ZnO (Cu/ZnO, NiO/ZnO, and Fe–ZnO) samples generally showed lower MB removal efficiencies, ranging from 74.86% to 92.1%, depending on the light source and catalyst dosage. This superior activity of C–ZnO–600 could be attributed to the synergistic effect of carbon incorporation, which enhances visible-light absorption and promotes charge separation efficiency. Overall, these results demonstrate that the synthesized C–ZnO–600 possesses excellent photocatalytic potential and could be considered a promising candidate for the degradation of dye pollutants in aqueous environments.

Table 1: Photocatalytic performance toward MB degradation of C-ZnO-600 compared with other catalysts

Material	Conditions					Light source	H(%)	Ref.
	Calcination temperature	Calcination time	Catalyst dosage	MB concentration	pH			
ZnO	500ºC	3 h	300 g		11	Sunlight	99.99	[36]
Cu/ ZnO	-	-	100 mg/L		-	Sunlight	92.1	[37]
ZnO	600ºC	-	50 g	10 mg/L	5	UV	81.5	[38]
NiO/ZnO	-	-	180 mg		-	UV	74.86	[39]
2%Fe–ZnO	-	-	10 mg/L		2	Sunlight	92	[40]
C-ZnO-600	600ºC	6 h	50 mg		11	UV	99.75	This word

3.2.2. Reusability and radical scavenger study

The reusability of the C–ZnO–600 photocatalyst was evaluated over five consecutive MB degradation cycles under UV irradiation (Figure 12a). The catalyst maintained a high degradation efficiency of about 80% after the first cycle and retained more than 73% activity even after five runs, indicating

excellent structural stability and photochemical durability. The slight decrease in efficiency may be attributed to surface fouling by adsorbed intermediates or partial loss of active sites during the washing process. Nevertheless, the minimal decline confirms that the C–ZnO composite possesses sufficient robustness for repeated use, making it a promising and sustainable photocatalyst for wastewater treatment.

To gain insight into the reactive species involved, various radical scavengers were employed (Figure 12b). The addition of $AgNO_3$, a known electron scavenger, caused only a slight decrease in degradation efficiency, indicating that electrons play a minor role in the photocatalytic process. In contrast, the degradation efficiency significantly decreased in the presence of isopropanol (IPA) and EDTA, which are scavengers for •OH radicals and holes (h^+), respectively. This observation confirms that •OH radicals and photogenerated holes are the primary oxidative species responsible for MB degradation. Meanwhile, benzoquinone (BQ), a scavenger of $•O_2^-$ radicals, showed a less pronounced effect, suggesting that $•O_2^-$ contributes to a lesser extent.

Based on these findings, a possible mechanism for MB degradation by C–ZnO under UV light can be proposed. Upon UV irradiation, ZnO generates electron–hole pairs (e^-/h^+). The photogenerated holes in the valence band oxidize surface hydroxyl groups or adsorbed H_2O molecules to produce •OH radicals, which act as the main oxidants for MB decomposition. Simultaneously, some photogenerated electrons in the conduction band may reduce O_2 to a small amount of $•O_2^-$ radicals, further assisting in degradation. The carbon layer derived from the rambutan-peel extract facilitates charge separation and transfer, suppressing electron–hole recombination and maintaining high photocatalytic stability during repeated cycles.

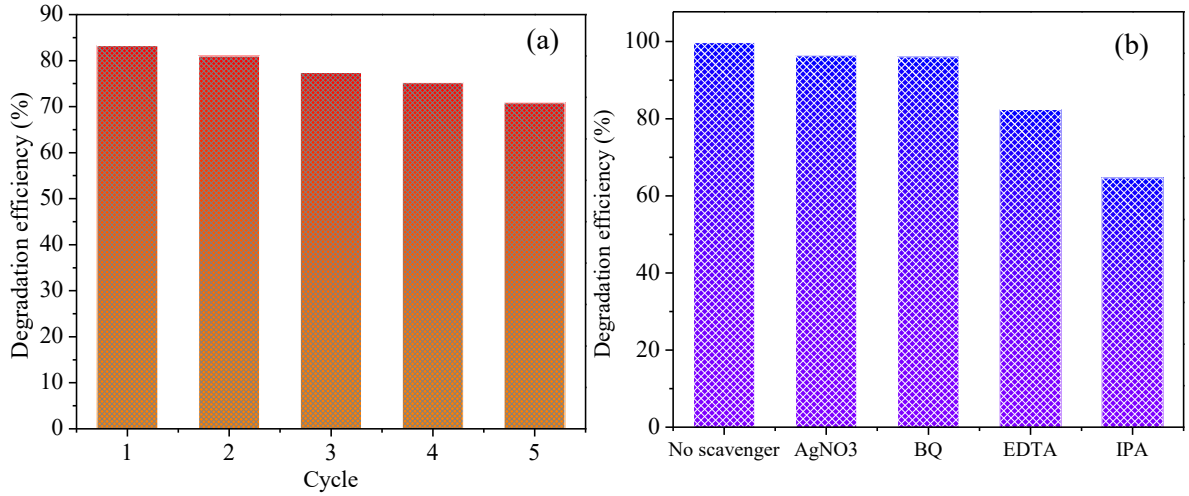

Figure 12: (a) Reusability of the photocatalyst for MB degradation over five consecutive cycles. (b) Effect of different radical scavengers on the MB photodegradation efficiency

3.3. Photocatalytic mechanism and DFT calculations

The optical absorption properties and band gap energies of the C–ZnO samples calcined at different temperatures were evaluated using UV–Vis diffuse reflectance spectroscopy (DRS), as shown in Figure 13. All samples exhibited a strong absorption edge in the UV region, corresponding to the intrinsic band–to–band transition of ZnO. The absorption edges were observed at approximately 375, 362, and 373 nm for C–ZnO–400, C–ZnO–600, and C–ZnO–800, respectively. In addition, a noticeable tail extending toward the visible region was observed, particularly for the C–ZnO–600 sample, suggesting the presence of defect levels or carbon-related mid-gap states introduced during the green synthesis using rambutan peel extract.

The optical band gap (E_g) values determined from the Tauc plots were 3.11 eV (C–ZnO–400), 2.76 eV (C–ZnO–600), and 3.08 eV (C–ZnO–800). The slight reduction in Eg for C–ZnO–600 indicates that moderate carbon incorporation and oxygen vacancies effectively narrow the band gap, thereby improving visible-light absorption. In contrast, the increase in Eg for the sample calcined at 800 °C can be attributed to the removal of residual carbon and the reduction of lattice defects due to improved crystallinity at high temperature. These findings suggest that the C–ZnO–600 photocatalyst possesses an optimal balance between structural order and defect concentration, which is beneficial for enhancing light-harvesting capability and photocatalytic performance under visible-light irradiation.

Such band gap modulation through green carbon doping not only tailors the electronic structure of ZnO but also facilitates more efficient charge separation. Consequently, the C–ZnO–600 sample is expected to exhibit superior photocatalytic activity compared to the other samples.

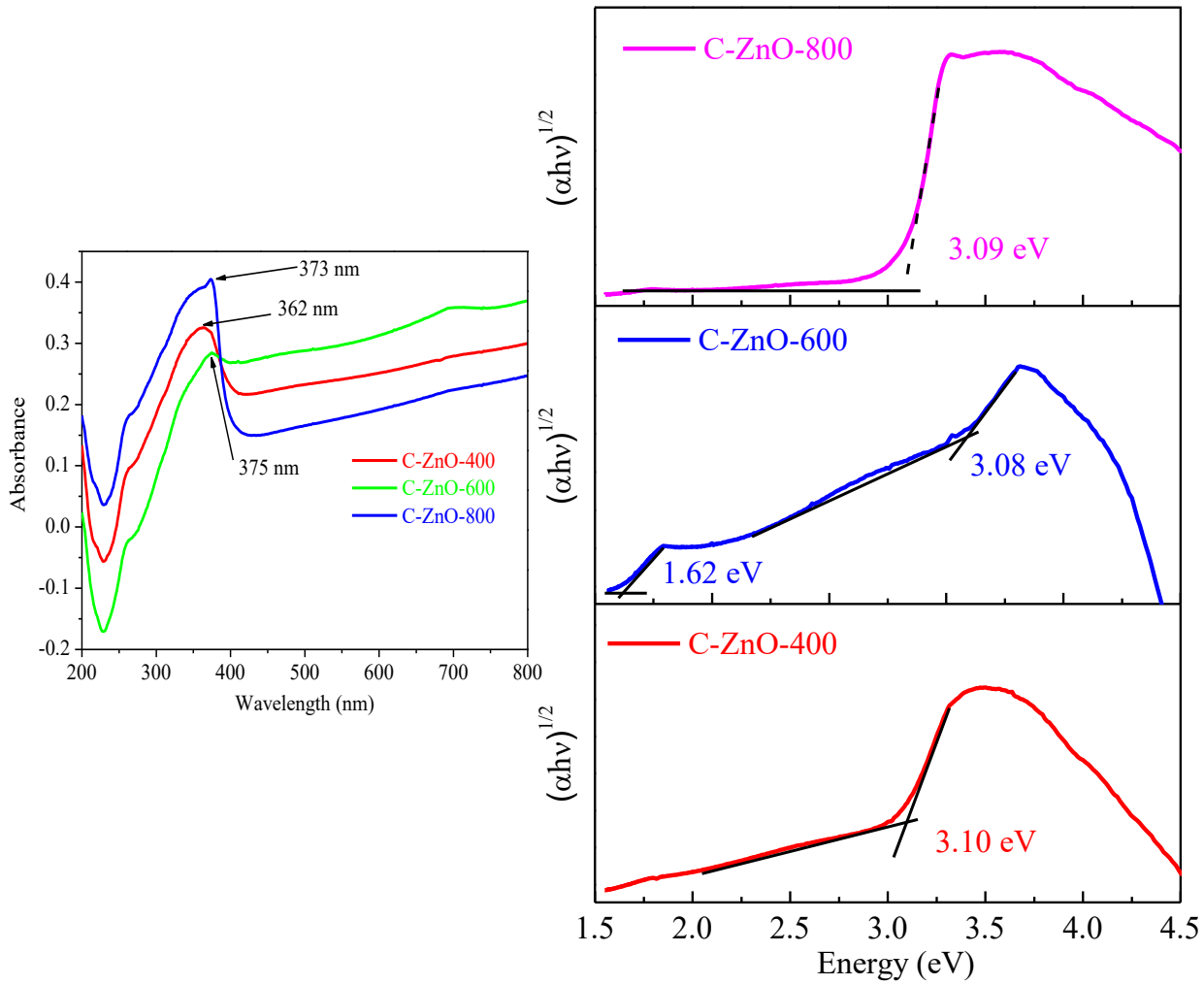

Figure 13. (a) UV–vis DRS spectra and (b) Tauc plot of materials

In order to investigate the electronic band structure and photocatalytic mechanism of the C-doped ZnO sample, the absolute electronegativity (χ) of the material was first determined based on the atomic fractions of Zn, O, and C obtained from EDS analysis. The calculation was performed using Equation (2):

$$\chi = (x_{Zn}\chi_{Zn} + x_{O}\chi_{O} + x_{C}\chi_{C}) \quad (2)$$

where x_i represents the atomic fraction of element i in the composite. Based on the EDS composition (Zn: 33.6%, O: 44.79%, C: 21.61%), and the absolute electronegativities of Zn (4.10 eV), O (7.54 eV), and C (5.30 eV), the value of χ is calculated by the Equation (2) is 5.90 eV.

The valence band (EVB) and conduction band (ECB) edge potentials of a semiconductor can be theoretically estimated based on the following empirical Equations (3) and (4):

$$E_{VB} = \chi - E_E + \frac{1}{2}E_g \quad (3)$$

$$E_{CB} = E_{VB} - E_g \quad (4)$$

where E_E= 4.50 eV is the energy of free electrons on the hydrogen scale [41] and E_g= 3.08 eV is the optical band gap from UV–DRS analysis. The corresponding potentials of the valence and conduction bands were calculated to be $E_{VB} = 2.94$ eV and $E_{CB} = -0.14$ eV, respectively.

The obtained band positions indicate that the conduction band potential of the C-doped ZnO is more negative (higher reducing ability) than the redox potential of $O_2/\bullet O_2^-$ (−0.33 eV vs. NHE), while the valence band potential is more positive (higher oxidizing ability) than that of $H_2O/\bullet OH$ (2.28 eV vs. NHE) [42]. Therefore, the photogenerated electrons in the conduction band can readily reduce O_2 to superoxide radicals ($\bullet O_2^-$), and the photogenerated holes in the valence band can oxidize water or hydroxide ions to produce hydroxyl radicals (•OH). Moreover, under alkaline conditions, the $OH^-/\bullet OH$ redox potential (2.28 eV) lies well below the valence band potential, further favoring the generation of •OH radicals. These results confirm that the C incorporation into the ZnO lattice effectively modulates the band structure, enhancing charge separation and promoting the simultaneous formation of both $\bullet O_2^-$ and •OH species, thereby improving photocatalytic activity under visible-light irradiation.

The DFT-calculated band structures and density of states (Fig. 14 (a,b)) provide a comprehensive understanding of the influence of carbon incorporation on the electronic configuration of ZnO. The pristine ZnO exhibits a well-defined separation between the valence band maximum (VBM) and conduction band minimum (CBM), consistent with its wide-bandgap semiconducting nature and relatively low intrinsic conductivity. Upon carbon doping, additional electronic states emerge close to the Fermi level, leading to an evident narrowing of the bandgap. This phenomenon can be ascribed to the hybridization between C 2p and O 2p orbitals, which modifies the charge density distribution and introduces mid-gap defect states [43]. Such an electronic rearrangement agrees well with the experimental UV–Vis DRS results, where the C-doped ZnO sample displays a redshift in the absorption edge and a lower optical bandgap compared with pristine ZnO.

The DOS spectra further demonstrate a substantial increase in the density of states near the Fermi energy after doping, indicating enhanced charge carrier density and improved electronic transport [44]. These modifications facilitate photoinduced charge separation and strengthen light absorption in the visible region, thereby improving the photocatalytic efficiency of the material.

It is noteworthy that the calculated bandgap energy for the C-doped ZnO model is smaller than the experimental value. This deviation is typically attributed to the use of an idealized crystalline structure in DFT simulations, which omits intrinsic defects, vacancies, and surface disorder commonly present in real materials. Moreover, the actual samples may contain coexisting heteroatoms or interstitial species that influence the band alignment [45]. Despite this discrepancy, the computational findings remain in strong

agreement with experimental observations, confirming that carbon doping effectively tunes the electronic structure of ZnO and enhances its photocatalytic performance.

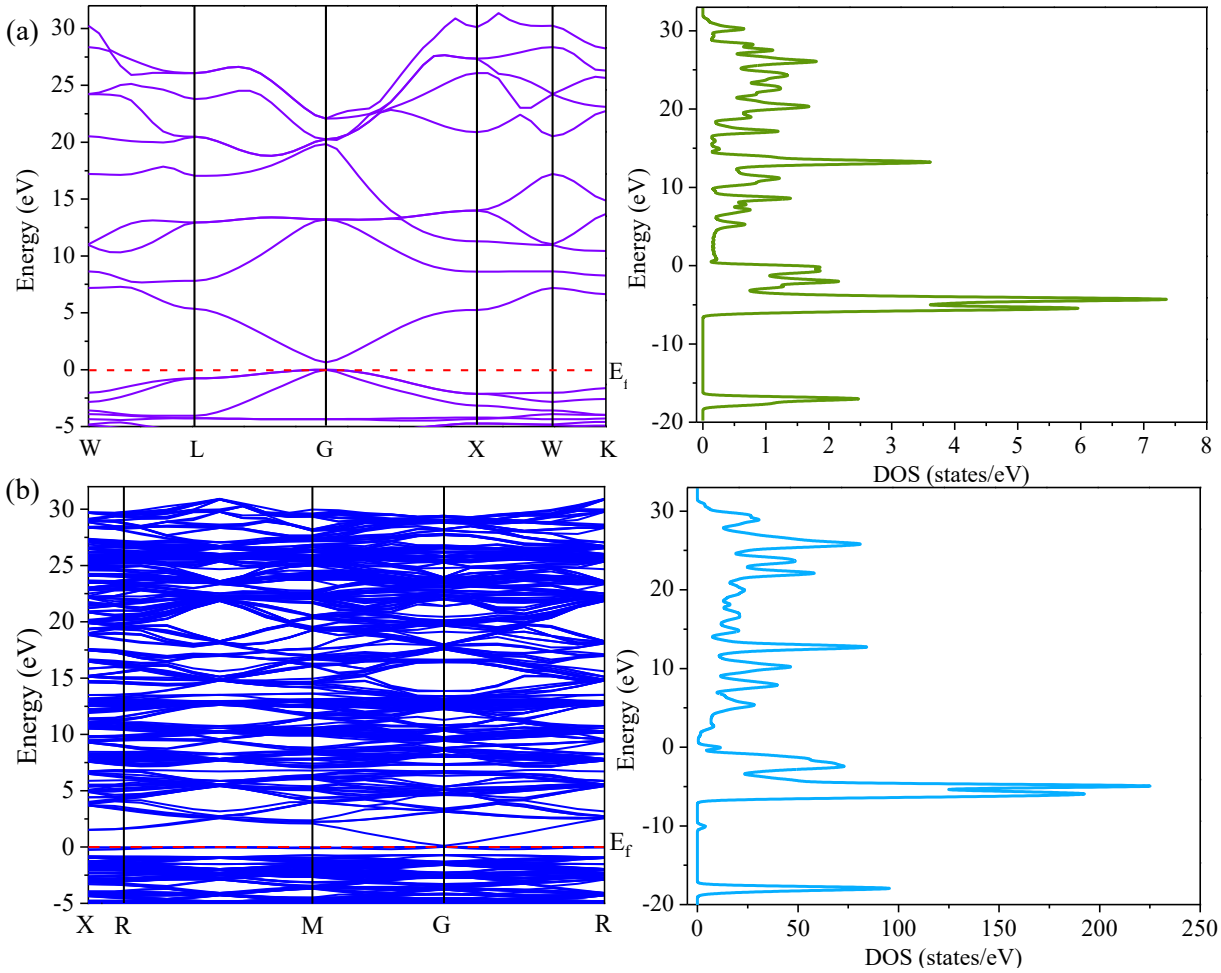

Figure 14: Calculated band structure and density of states (DOS) of (a) pristine ZnO and (b) C–ZnO–600 using DFT

Figure 15 shows the charge density difference map clearly shows that carbon incorporation causes a remarkable redistribution of electronic charge within the ZnO lattice. The yellow regions represent charge accumulation, while the blue regions indicate charge depletion. Around the doped carbon site, a significant accumulation of charge density is observed, particularly between the C and adjacent O atoms, implying the formation of strong covalent C–O bonds [46]. This hybridization leads to partial electron transfer from neighboring Zn atoms toward the C site, modifying the local electrostatic environment of the lattice.

Such redistribution indicates that carbon acts as an electron-rich dopant, introducing localized states and enhancing the electronic polarization of the ZnO matrix. This charge reorganization facilitates the separation of photoinduced electron–hole pairs and improves the conductivity of the material. The formation of C–O hybrid orbitals also contributes to bandgap narrowing, which is consistent with the DFT

and experimental UV–Vis DRS results. Overall, carbon doping effectively tailors the electronic charge distribution of ZnO, resulting in improved charge transfer dynamics and enhanced photocatalytic activity.

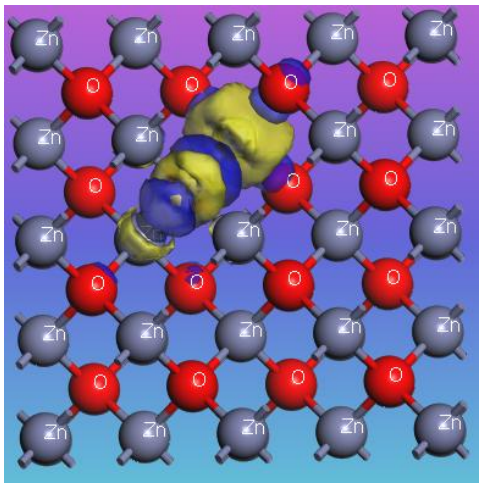

Figure 16: Charge density maps of C–ZnO–600

The proposed photocatalytic mechanism of C–ZnO–600 is illustrated in Figure 17. Upon UV irradiation, electrons in the valence band (VB) are promoted to the conduction band (CB), leaving holes in the VB. The carbon incorporation introduces mid-gap states around 1.62 eV, which enable sub-band-gap excitation and improve charge transfer efficiency. However, since the CB potential of C–ZnO–600 is less negative than the redox potential of $O_2/\bullet O_2^-$ (−0.33 V vs NHE), the photogenerated electrons cannot effectively reduce O_2 to $\bullet O_2^-$. Instead, these electrons are likely captured by the defect-related energy levels, reducing recombination and extending carrier lifetime. Meanwhile, the photogenerated holes exhibit sufficient oxidation potential to react with surface hydroxyl groups or water, generating •OH radicals with strong oxidizing ability. These reactive species play a crucial role in attacking and decomposing methylene blue (MB) molecules into smaller intermediates and ultimately mineralized products. The synergistic effects of carbon doping and defect-state formation thus contribute to enhanced light utilization and improved photocatalytic efficiency.

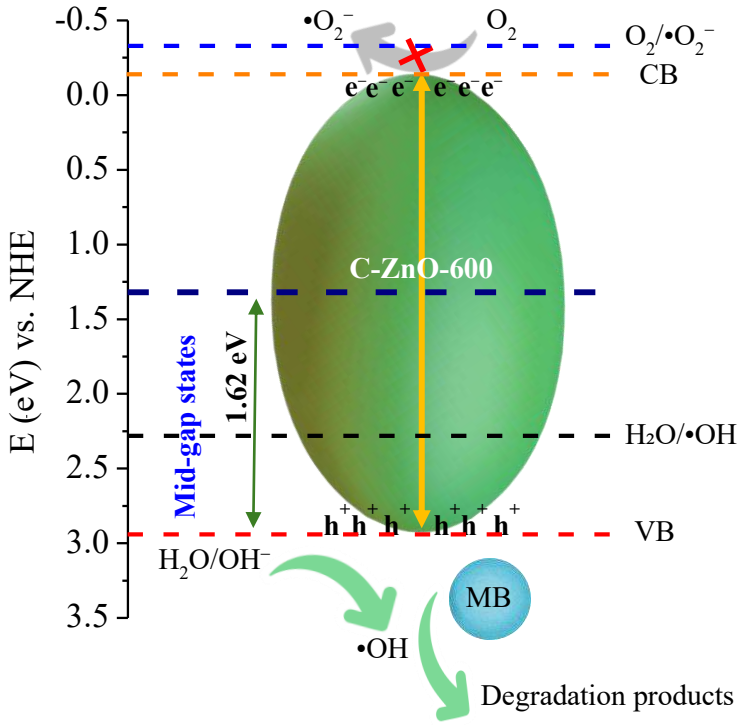

Figure 16: Possible photocatalytic mechanism of C–ZnO–600 for the degradation of MB

4. Conclusion

Carbon-doped ZnO nanoparticles were successfully synthesized using rambutan peel extract through an environmentally friendly route that simultaneously achieved waste valorization and material enhancement. The optimal C–ZnO–600 sample exhibited the highest photocatalytic activity, achieving up to 82% degradation of methylene blue after 180 min of UV irradiation, following pseudo-first-order kinetics. The superior performance was attributed to the synergistic effects of moderate carbon incorporation, suitable crystallinity, and enhanced charge separation efficiency. Radical trapping experiments confirmed that •OH radical was the main oxidative species responsible for dye degradation. DFT simulations supported the experimental results, indicating that carbon doping introduced mid-gap states, narrowed the band gap, and improved charge transport through C–O hybridization. Overall, this green synthesis strategy not only provides a sustainable route for producing high-performance photocatalysts but also contributes to circular economy principles by utilizing agricultural waste for environmental remediation.

Acknowledgments

The authors acknowledge support from the Faculty of Chemical Engineering and Food Technology, Nong Lam University HCMC and Faculty of Biological Sciences, Research Institute for Biotechnology and Environment, Nong Lam University HCMC.

Funding

No funding

Ethical approval

Not applicable.

Consent to participate

Not applicable.

Consent for publication

All authors have studied the manuscript thoroughly and consented to the publication.

Competing interests

The authors declare no competing interests.

References

[1] S. Selvaraj, D.S. Patrick, V.S. Manikandan, G.A. Vangari, M.K. Mohan, M. Navaneethan, Synergistic effects of La-doping on ZnO nanostructured photocatalysts for enhanced MB dye degradation, Surfaces and Interfaces 51 (2024) 104538. https://doi.org/10.1016/j.surfin.2024.104538.

[2] S. Choudhary, K. Sharma, V. Kumar, V. Sharma, RSM-CCD directed modeling and optimization of a low-cost adsorbent based on sodium dodecyl sulfate for the selective removal of malachite green and methylene blue dyes: Kinetics, isotherm, and thermodynamics analysis, Microchemical Journal 205 (2024) 111158. https://doi.org/10.1016/j.microc.2024.111158.

[3] S.S. Emmanuel, A.A. Adesibikan, Bio-fabricated green silver nano-architecture for degradation of methylene blue water contaminant: A mini-review, Water Environment Research 93 (2021) 2873–2882. https://doi.org/10.1002/wer.1649.

[4] X. Fan, X. Liu, Y. Wang, Low-cost and resource-efficient monolithic photocatalyst with enhanced solar light utilization for the photocatalytic treatment of organic wastewater, Chemosphere 312 (2023) 137052. https://doi.org/10.1016/j.chemosphere.2022.137052.

[5] Y. Wang, R. Liu, M. Shi, P. Zhou, K. Han, C. Li, R. Li, Photo-induced carbon dioxide reduction on hexagonal tungsten oxide via an oxygen vacancies-involved process, Chinese Chemical Letters 34 (2023) 107200. https://doi.org/10.1016/j.cclet.2022.02.006.

[6] A. Alsalme, K.M.A. Elmoneim, N.N. Mohammed, K. Mohamed, M.F. Abdel-Messih, A. Sultan, M.A. Ahmed, Rational sonochemical synthesis of S-scheme Bi2O2CO3/ZnO heterojunction for photocatalytic expelling of harmful rhodamine B dye from wastewater under natural sunlight, Ceramics International 50 (2024) 50622–50634. https://doi.org/10.1016/j.ceramint.2024.09.407.

[7] G. Ahmed, W.S. Mohamed, M.F. Hasaneen, H.M. Ali, E.M.M. Ibrahim, Optical, structural, electrical and photocatalytic properties of aluminum doped zinc oxide nanostructures, Optical Materials 140 (2023) 113880. https://doi.org/10.1016/j.optmat.2023.113880.

[8] A.M. El-Khawaga, M.A. Elsayed, M. Gobara, A.A. Suliman, A.H. Hashem, A.A. Zaher, M. Mohsen, S.S. Salem, Green synthesized ZnO nanoparticles by Saccharomyces cerevisiae and their antibacterial activity and photocatalytic degradation, Biomass Conv. Bioref. 15 (2025) 2673–2684. https://doi.org/10.1007/s13399-023-04827-0.

[9] L.M. Huong, C.Q. Cong, N.M. Dat, N.D. Hai, N.T.H. Nam, H. An, L.T. Tai, T. Do Dat, N.T. Dat, M.T. Phong, N.H. Hieu, Green synthesis of carbon-doped zinc oxide using Garcinia mangostana peel extract: Characterization, photocatalytic degradation, and hydrogen peroxide production, Journal of Cleaner Production 392 (2023) 136269. https://doi.org/10.1016/j.jclepro.2023.136269.

[10] C. Karaca, Z. Eroğlu, S. Karaca, Anthraquinone-rich Rheum ribes L. as a source of nitrogen-doped carbon quantum dots for ZnO-based S-scheme heterojunction photocatalysts in tetracycline degradation, Journal of Environmental Chemical Engineering 13 (2025) 115999. https://doi.org/10.1016/j.jece.2025.115999.

[11] M.J. Sadiq Mohamed, M.A. Gondal, Nanostructured defects-rich black-ZnO/biowaste-derived carbon composites for efficient visible light-driven hydrogen generation: A study on the role of C–Zn@C–O–Zn interface, International Journal of Hydrogen Energy 92 (2024) 47–58. https://doi.org/10.1016/j.ijhydene.2024.10.152.

[12] A.S. Alqahtani, S. Elbeltagi, Advancing chemistry sustainably: From synthesis to benefits and applications of green synthesis, Journal of Organometallic Chemistry 1027 (2025) 123508. https://doi.org/10.1016/j.jorganchem.2025.123508.

[13] B. Qu, Z. Xiao, Y. Luo, Sustainable nanotechnology for food preservation: Synthesis, mechanisms, and applications of zinc oxide nanoparticles, Journal of Agriculture and Food Research 19 (2025) 101743. https://doi.org/10.1016/j.jafr.2025.101743.

[14] D.D. Suppiah, N.M. Julkapli, S. Sagadevan, M.R. Johan, Eco-friendly green synthesis approach and evaluation of environmental and biological applications of iron oxide nanoparticles, Inorganic Chemistry Communications 152 (2023) 110700. https://doi.org/10.1016/j.inoche.2023.110700.

[15] S. Babulla, A.M. Kumari, M.S. Chandra, N.R. Maddela, R. Prasad, Phytosynthesized manganese oxide nanoparticles using Pterocarpus santalinus: Characterization and its role in antioxidant, antimicrobial, and seed priming efficacy, Biocatalysis and Agricultural Biotechnology 69 (2025) 103790. https://doi.org/10.1016/j.bcab.2025.103790.

[16] P. Bhattacharjee, S. Das, S.K. Das, S. Chander, Rambutan (Nephelium lappaceum L.): A potential fruit for industrial use, serving nutraceutical and livelihood interests and enhancing climate resilience, South African Journal of Botany 150 (2022) 26–33. https://doi.org/10.1016/j.sajb.2022.06.064.

[17] V. Thamilselvan, S. Balu, D. Ganapathy, R. Atchudan, S. Arya, S. Hazra, A.K. Sundramoorthy, Utilization of biomass waste derived carbon quantum dots intercalated ZnO for effective photocatalytic degradation of methylene blue, Results in Surfaces and Interfaces 19 (2025) 100520. https://doi.org/10.1016/j.rsurfi.2025.100520.

[18] Q. Lin, Z. Liu, H. Dong, X. Zhou, Theoretical insights into BiVO4/ZnO heterojunction photocatalyst: interfacial charge separation, band alignment, and reaction mechanism, Journal of Photochemistry and Photobiology A: Chemistry 473 (2026) 116840. https://doi.org/10.1016/j.jphotochem.2025.116840.

[19] N. Sedefoglu, Characterization and photocatalytic activity of ZnO nanoparticles by green synthesis method, Optik 288 (2023) 171217. https://doi.org/10.1016/j.ijleo.2023.171217.

[20] D.E. Yizengaw, E.M. Godie, A.H. Manayia, Green synthesis and characterization of ZnO nanoparticles using Justicia Schemperiana leaf extract and its antibacterial and antioxidant activity, Inorganic Chemistry Communications 174 (2025) 114071. https://doi.org/10.1016/j.inoche.2025.114071.

[21] I.M. Khaled, M. Umair, C.M. Pecoraro, A. Kheniche, M. Bellardita, S. Soltani, Green synthesis of ZnO and CuO nanoparticles and ZnO-CuO nanocomposites: Characterization and photocatalytic dyes removal efficiency's determination, Colloids and Surfaces A: Physicochemical and Engineering Aspects 728 (2026) 138544. https://doi.org/10.1016/j.colsurfa.2025.138544.

[22] A. Nandhini, P. Anilkumar, J. Jasmin, S. Balamurali, Green synthesis, characterization, structural, morphological, antibacterial, and cytotoxicity evaluation of zinc oxide nanoparticles using Fioria vitifolia extract, Biophysical Chemistry 323 (2025) 107440. https://doi.org/10.1016/j.bpc.2025.107440.

[23] D. Quang Trung, M.T. Tran, N.V. Du, N.D. Hung, T. Thi Hao Tam, N. Tu, P. Minh Tri, H. Gia Chuc, N.D. Trung Kien, N. Van Quang, P.T. Huy, Highly efficient and thermally stable cyan-emitting ZnS/ZnO phosphors for full-visible-spectrum LED lighting, RSC Adv. 15 (2025) 616–627. https://doi.org/10.1039/D4RA08038F.

[24] J.J. Beltrán, C.A. Barrero, A. Punnoose, Relationship between ferromagnetism and formation of complex carbon bonds in carbon doped ZnO powders, Phys. Chem. Chem. Phys. 21 (2019) 8808–8819. https://doi.org/10.1039/C9CP01277J.

[25] N. Srinivasan Alias Arunsankar, M. Anbuchezhiyan, S. Padmaja, Enhanced photocatalytic mineralization efficiency of anionic element doped ZnO by improving separation of excitons, J Mater Sci: Mater Electron 32 (2021) 12631–12647. https://doi.org/10.1007/s10854-021-05899-2.

[26] L. Jing, P. Li, Z. Li, D. Ma, J. Hu, Influence of π–π interactions on organic photocatalytic materials and their performance, Chem. Soc. Rev. 54 (2025) 2054–2090. https://doi.org/10.1039/D4CS00029C.

[27] Md. Ahmaruzzaman, Metal oxides (ZnO, CuO and NiO)-based nanostructured materials for photocatalytic remediation of organic contaminants, Nanotechnol. Environ. Eng. 8 (2023) 219–235. https://doi.org/10.1007/s41204-022-00284-8.

[28] C.T. Quy, N.X. Thai, N.D. Hoa, D.T. Thanh Le, C.M. Hung, N. Van Duy, N. Van Hieu, C_2H_5OH and NO_2 sensing properties of ZnO nanostructures: correlation between crystal size, defect level and sensing performance, RSC Adv. 8 (2018) 5629–5639. https://doi.org/10.1039/C7RA13702H.

[29] T.T.T. Huong, N.T. Sa, N.T.M. Thuy, P.V. Hao, N.H. Thao, N.T. Hien, N.X. Ca, Eu^{3+} -doped ZnO quantum dots: structure, vibration characteristics, optical properties, and energy transfer process, Nanoscale Adv. 7 (2025) 909–921. https://doi.org/10.1039/D4NA00858H.

[30] G.H. Mhlongo, K. Shingange, Z.P. Tshabalala, B.P. Dhonge, F.A. Mahmoud, B.W. Mwakikunga, D.E. Motaung, Room temperature ferromagnetism and gas sensing in ZnO nanostructures: Influence of intrinsic defects and Mn, Co, Cu doping, Applied Surface Science 390 (2016) 804–815. https://doi.org/10.1016/j.apsusc.2016.08.138.

[31] L.M. Huong, N.M. Dat, N.T. Hoai Nam, H. An, N.D. Hai, P.N. Phu Hung, N.C. Anh Minh, N.H. Vu, L.T. Nhiem, N.T. Thang, N.H. Hieu, Enhanced sunlight-driven photocatalysis of non-metal doped zinc oxide via wet impregnation for the removal of organic compounds, Environmental Nanotechnology, Monitoring & Management 22 (2024) 100990. https://doi.org/10.1016/j.enmm.2024.100990.

[32] N.Q.T. Ton, T.N.T. Le, S. Kim, V.A. Dao, J. Yi, T.H.T. Vu, High-Efficiency Photo-Generated Charges of ZnO/TiO_2 Heterojunction Thin Films for Photocatalytic and Antibacterial Performance, J Nanosci Nanotechnol 20 (2020) 2214–2222. https://doi.org/10.1166/jnn.2020.17306.

[33] N. Sedefoglu, Green synthesis of ZnO nanoparticles by Myrtus communis plant extract with investigation of effect of precursor, calcination temperature and study of photocatalytic performance, Ceramics International 50 (2024) 9884–9895. https://doi.org/10.1016/j.ceramint.2024.01.387.

[34] D. Zhang, F. Zeng, Visible light-activated cadmium-doped ZnO nanostructured photocatalyst for the treatment of methylene blue dye, J Mater Sci 47 (2012) 2155–2161. https://doi.org/10.1007/s10853-011-6016-4.

[35] S. Senda, Influence of Cu on the photocatalytic activity of ZnS nanoparticles, in: AIP Conference Proceedings, AIP, Sendai (Japan), 2006: pp. 65–68. https://doi.org/10.1063/1.2207075.

[36] M.E. Cervantes-Gaxiola, F.A. Vázquez-González, E.Y. Rios-Iribe, P.F. Méndez-Herrera, C. Leyva, Effect of pH on the green synthesis of ZnO nanoparticles using Sorghum bicolor seed extract and their application in photocatalytic dye degradation, Materials Letters 372 (2024) 136982. https://doi.org/10.1016/j.matlet.2024.136982.

[37] S.M. Sajjadi, G. Hossinzadeh, Textile dyes removing from the wastewater by green synthesized Cu-doped ZnO photocatalysts under the simulated sunlight illumination, Ceramics International 50 (2024) 36271–36285. https://doi.org/10.1016/j.ceramint.2024.07.011.

[38] I. Riwayati, S. Winardi, S. Madhania, M. Shimada, Kusdianto, Green synthesis of ZnO nanoparticles using Cosmos caudatus: Effects of calcination temperature and precursor type on photocatalytic and antimicrobial activities, Results in Engineering 24 (2024) 103594. https://doi.org/10.1016/j.rineng.2024.103594.

[39] K.A. Isai, V.S. Shrivastava, Photocatalytic degradation of methylene blue using ZnO and 2%Fe–ZnO semiconductor nanomaterials synthesized by sol–gel method: a comparative study, SN Appl. Sci. 1 (2019) 1247. https://doi.org/10.1007/s42452-019-1279-5.

[40] K.A. Isai, V.S. Shrivastava, Photocatalytic degradation of methylene blue using ZnO and 2%Fe–ZnO semiconductor nanomaterials synthesized by sol–gel method: a comparative study, SN Appl. Sci. 1 (2019) 1247. https://doi.org/10.1007/s42452-019-1279-5.

[41] O.A. Oyewo, S. Ramaila, L. Mavuru, Adsorption and photocatalytic removal of murexide using ZnO/rGO and ZnO/g-C3N4 composites, Inorganic Chemistry Communications 151 (2023) 110601. https://doi.org/10.1016/j.inoche.2023.110601.

[42] B. Tatykayev, F. Donat, H. Alem, L. Balan, G. Medjahdi, B. Uralbekov, R. Schneider, Synthesis of Core/Shell ZnO/rGO Nanoparticles by Calcination of ZIF-8/rGO Composites and Their Photocatalytic Activity, ACS Omega 2 (2017) 4946–4954. https://doi.org/10.1021/acsomega.7b00673.

[43] A.S. Alshammari, L. Chi, X. Chen, A. Bagabas, N. Rashidi-Alavijeh, D. Kramer, A. Alromaeh, Z. Jiang, Visible-light photocatalysis on C-doped ZnO derived from polymer- assisted pyrolysis, (n.d.).

[44] C. Wang, T. Xu, K. Gao, L. Jin, C. Guo, W. Wang, Y. Hu, Carbon doping synergistically regulates carrier separation kinetics and elementary reaction thermodynamics for efficient CO2 photoreduction on Zn-polar ZnO nanocobbles, Applied Catalysis B: Environment and Energy 383 (2026) 126025. https://doi.org/10.1016/j.apcatb.2025.126025.

[45] L.M. Huong, L.T. Tai, N.M. Dat, N.D. Hai, H. An, N.T.H. Nam, T. Thi Thu Hanh, N.H. Hieu, Non-metallic X (X = C, N, S, and P) co-doped copper oxide derived from Mangifera indica leaf extract: Synthesis, characterization, density functional theory simulation of structure, and photoactivities, Colloids and Surfaces A: Physicochemical and Engineering Aspects 687 (2024) 133393. https://doi.org/10.1016/j.colsurfa.2024.133393.

[46] D.A. Oluwasogo, S. Varangane, Y.T. Prabhu, B.M. Abraham, V. Perupogu, U. Pal, Biosynthetic modulation of carbon-doped ZnO for rapid photocatalytic endocrine disruptive remediation and hydrogen evolution, Journal of Cleaner Production 394 (2023) 136393. https://doi.org/10.1016/j.jclepro.2023.136393.